Electronic Supplementary Information

Lithio-amphiphilic nanobilayer for high energy density anode-less all-solid-state batteries operating under low stack pressure

Jihoon Oh,[a,b] Seung Ho Choi,[c] Heejin Kim,[d] Ji Young Kim,[e] Geung-Jong Lee,[c] Ki Yoon Bae,[e] Taegeun Lee,[a,b] Nohjoon Lee,[a,b] Yeeun Sohn,[a,b] Woo Jun Chung,[a,b] and Jang Wook Choi*[a,b]

[a.] *School of Chemical and Biological Engineering and Institute of Chemical Process, Seoul National University, 1 Gwanak-ro, Gwanak-gu, Seoul 08826, Republic of Korea. E-mail: jangwookchoi@snu.ac.kr*
[b.] *Hyundai Motor Group-Seoul National University (HMG-SNU) Joint Battery Research Center (JBRC), Seoul National University, Seoul, Republic of Korea*
[c.] *Advanced Batteries Research Center, Korea Electronics Technology Institute, Seongnam, Republic of Korea*
[d.] *Division of Analytical Science, Korea Basic Science Institute, Daejeon, Republic of Korea*
[e.] *Advanced Battery Development Team, Hyundai Motor Company, Hwaseong, Republic of Korea*
† Electronic Supplementary Information (ESI) available: See DOI: 10.1039/x0xx00000x

Experimental Section

Preparation of electrode. The Mg electrode was fabricated by sputtering elemental Mg on a 20 μm-thick SUS or 10 μm-thick Ni current collector. The 10 μm-thick Ni foil was exclusively utilized for the pouch-type full-cells, whereas SUS foil was employed in all other assessments. Fabrication of the W/Mg electrode involved the additional deposition of a layer of W on the Mg electrode, with the thicknesses of the W and Mg layers set to 30 and 200 nm, respectively. The W(200 nm)/Mg(200 nm) electrode was produced using the same procedure, but the thickness of the W layer was adjusted to 200 nm. The W(30 nm)/Mg(0 nm) electrode was fabricated by depositing only a 30 nm-thick layer of W on SUS. The composite cathode utilized for the full-cell evaluations was prepared by dispersing $LiNbO_3$-coated NCM811, LPSCl, vapor-grown carbon fiber (VGCF), and butadiene rubber (BR) binder in butyl butyrate in a weight ratio of 82:15.5:1:1.5. This mixture was then cast on Al foil and dried at 100 °C for 15 hours.

Characterization methods. XRD patterns of the pristine anode-less electrodes were acquired using a high-resolution X-ray diffractometer (SmartLab, Rigaku). XPS analyses were conducted with an X-ray photoelectron spectrometer system (Nexsa, Thermo Fisher Scientific). Top- and cross-sectional images of the electrodes were captured using field emission scanning electron microscopy (FE-SEM, JSM-7800F Prime, JEOL) and focused ion beam (FIB) (Helios 650, FEI), respectively. The 3D morphology of the interfaces in each cell was analyzed using the integrated high-resolution 3D XRM and computed tomography system (Xradia 620 Versa, Carl Zeiss) installed at the National Center for Inter-University Research Facilities (NCIRF) at Seoul National University. In this analysis, the anode-SE interface was selectively exposed to X-ray beams for 8 hours under the following conditions: 80 kV (voltage), 125 μA (current), and 10 W (power). The image resolution was set to 0.5 pixels per unit. Subsequently, the raw data obtained were processed to reconstruct the 3D and 2D structures of the anode-SE interface using advanced imaging software (Dragonfly Pro Workstation Version 2021.1 Build 977, Object Research Systems). The SE mappings were conducted using 3D view mode and ISO render mode. The pore intensity in the samples was

color-scaled with a 3D Look Up Table (LUT) in the contrast window from 12,000 to 35,000 using the same software.

Computational details. Density functional theory (DFT) calculations were performed using the Vienna Ab initio Simulation Package (VASP) software[1] and the Perdew-Burke-Ernzerhof (PBE) exchange-correlation functional[2] and projector-augmented wave method[3]. An energy cutoff of 520 eV and a Monkhorst-Pack k-point mesh with a grid spacing of 0.03 $Å^{-1}$ were used. The convergence criteria for electronic and ionic relaxations were 10^{-7} eV and 0.02 eV $Å^{-1}$, respectively. The linear extrapolation scheme proposed in a previous study[4] was used to evaluate the interface energy. Computational details for modeling the interface between Li metal and the target materials are presented in Note S1–S3, ESI†.

Electrochemical characterization. The assembly of all-solid-state half-cells commenced with the pelletization of 100 mg of LPSCl to form an SE layer with a diameter of 10 mm through cold pressing at 120 MPa. Subsequently, the anode-less electrode was positioned beneath the SE layer, and the assembled cell underwent compression at 390 MPa. Li foil was placed atop the SE layer, with SUS foils serving as current collectors for both electrodes. The cell assembly was then placed in a custom-fabricated housing case for pressure control during testing. A precise pressure of 15 MPa was maintained by integrating a spring with a specific spring constant (Shinheung Indus.) and depth adjustment. All-solid-state full-cells were produced by preparing the SE layer using the same method as for the half-cells. The cathode and anode-less electrode were positioned on each side of the SE pellet, and the entire assembly was compressed at 390 MPa. Following compression, the cell was inserted into a housing case with a spring, and a stack pressure of 15 MPa was applied using the same procedure as for the half-cells. All components were assembled within an argon-filled glove box. All electrochemical assessments were carried out at 25 °C. The stripping cutoff voltage of all half-cell tests was set at 0.1 V (vs. Li/Li^+), utilizing the battery cycler (WBCS 3000, WonATech). The electrochemical performance of pellet-based full-cells was evaluated in constant current and constant voltage (CC/CV) mode for charge and constant current (CC) mode for discharge in the potential range of 2.5–4.2 V (vs Li/Li^+), using the same battery cycler as for half-cell evaluation. Pouch-type full-cells with low stack pressure were evaluated in CC mode for both

charge and discharge, with the charge cutoff set at 4.3 V. AC impedance measurements were conducted in a half-cell configuration within a frequency range from 1 MHz to 0.1 Hz.

Pouch-type full-cell fabrication. SE sheets containing LPSCl were prepared using BR as the binder in butyl butyrate. These materials were blended with ZrO_2 beads in a planetary centrifugal mixer (Thinky Corporation, AR-100). The resultant mixture was evenly coated onto a release polyethylene terephthalate (PET) film using the doctor blade process. The coated film was then dried on a hotplate at 60 °C for a few minutes, followed by additional drying in a vacuum oven at 40 °C overnight. The thickness of the SE sheet was measured to be 100 μm except for that of the cell presented in Fig. S28, ESI† (30 μm). All procedures were meticulously conducted in a dry room, in which the dew point was maintained below −50 °C. A pouch-cell, measuring 30 × 40 mm^2, was fabricated using the following steps: electrodes and SE sheets were precisely cut using a punching machine, and these components were systematically stacked and packed into a laminate bag. Subsequent to vacuum sealing the bag, it was pressurized at 450 MPa and 85 °C for 30 minutes using a warm isostatic press (WIP) (ISA-W50-6000, Ilshin Autoclave). The assembly process mostly occurred under controlled dry air atmosphere with a dew point below −50 °C. Notably, the isostatic press was used under ambient atmospheric conditions due to facility limitations.

Note S1 Calculation of interface between Li and bcc metals (W, Cr, Mo).

Since the bcc metals have the same crystal symmetry as Li metal, we assumed a coherent interface between Li metal and these transition metals (TMs). In the calculation, we used 4–6 TM layers and the number of Li layers was increased systematically. To validate this computation model, we tested larger models comprising 10 TM layers (thickness of ~20 Å), and obtained almost the same result (1.9% difference). The in-plane lattice parameters (*a*- and *b*- constants) were fixed to those of the TMs, and the lattice was allowed to relax in the direction normal to the interface (*c*- direction) because the Li metal layer may have a degree of freedom in the direction normal to the surface during growth. We also tested cases with fixed lattice parameters in all directions, and the energy differences were less than 5%. The low-index facets, (100), (110), and (111), were examined for all TMs. The {112} and {114} facets were additionally tested for the W|Li interface of interest, because those {11*x*} facets are perpendicular to the lowest energy surface (110), and also, they are facets with low-energy grain boundaries (e.g., Σ3(11–1)[110], Σ3(11–2)[110], and Σ3(11–4)[110]) that would be in contact with Li metal if the Li dendrites were to grow through such grain boundaries[5].

Note S2 Calculation of interface between Li and hcp metals (Ti, Zr).

We assumed that Li metal has a bcc structure in contact with hcp TMs. The TM(100)|Li(100), TM(110)|Li(100), and TM(001)|Li(100) interfaces were evaluated. We considered only the (100) facet of Li metal when creating the interface because the effect of the initial Li configuration on the interface energy is known to be insignificant in the linear extrapolation scheme[4]. We created rectangular supercells of the TMs (~10 x 10 Å in size) such that the lattice mismatch was as small as possible in the planar (*a*- and *b*-) direction when contacting the supercells of Li metal. Then, the *a*- and *b*- parameters of the Li layer were adjusted to match the TM lattice. The initial position of the Li layer in the *a*- and *b*- directions was systematically tested at 4 x 4 grid positions, and the most stable one was selected. As in the case of the bcc TMs, the *a*- and *b*- lattice constants were fixed to those of the TMs, and the lattice was relaxed only in the direction normal to the interface (*c*- direction).

Note S3 Calculation of interface between Li and ionic compounds (Li_6PS_5Cl, Li_2S, LiF).

As in the case of the hcp TMs, we considered the interface between the low-index facets of the ionic compounds and the (100) facet of the bcc Li metal. For the low-index facets of the ionic compounds, we prepared all possible stoichiometric cutting planes of the (100), (110), and (111) facets. Then, the most stable slab models for each facet were evaluated to construct the interface with the Li metal. The remaining calculation procedures were identical to those ones used for the hcp metals.

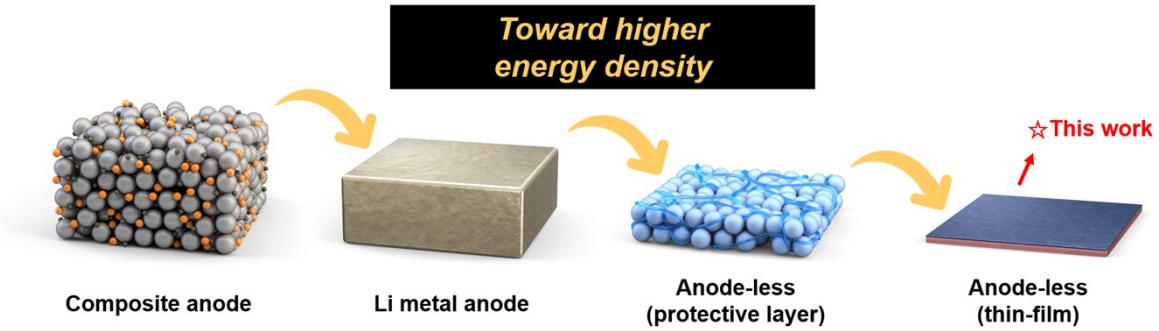

Fig. S1 Evolution of anode schemes in ASSBs with regard to volumetric energy density. The thin-film-based approach in this study maximizes the volumetric energy density.

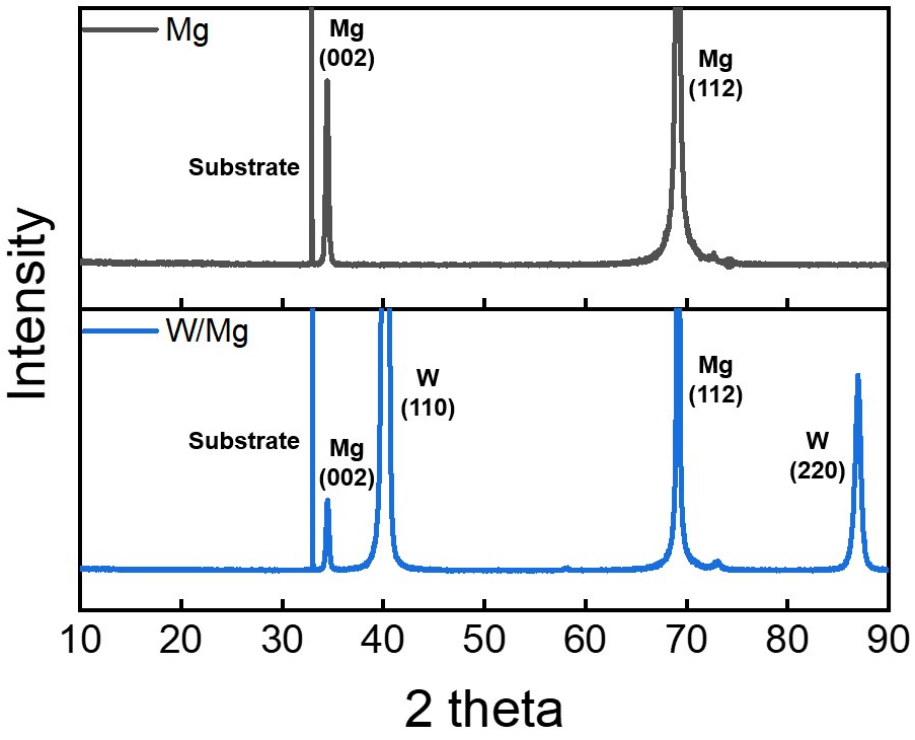

Fig. S2 XRD patterns of Mg and W/Mg thin-films.

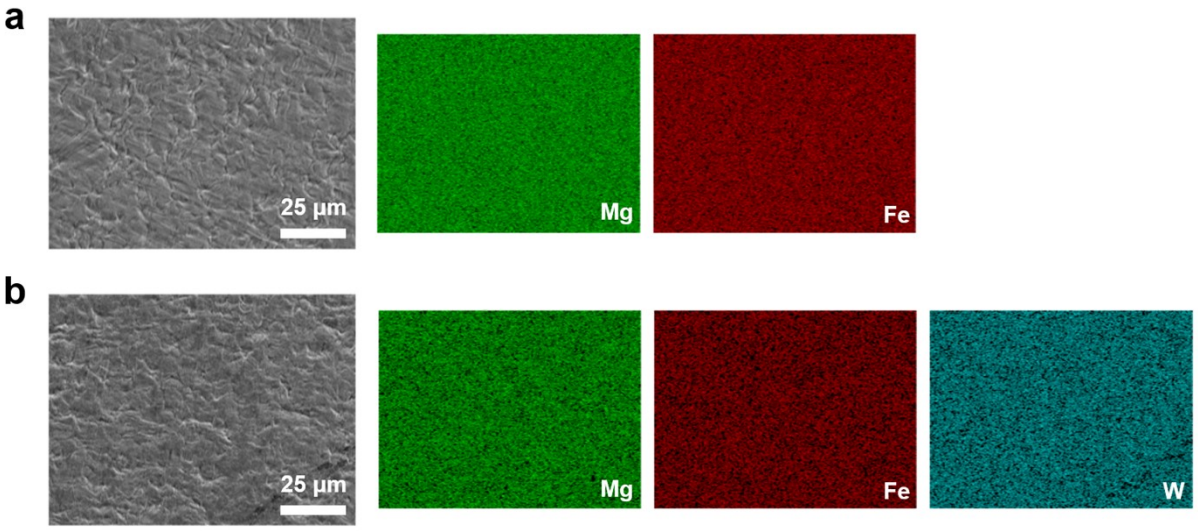

Fig. S3 Top-view SEM-EDS images of (a) Mg and (b) W/Mg thin-film electrodes.

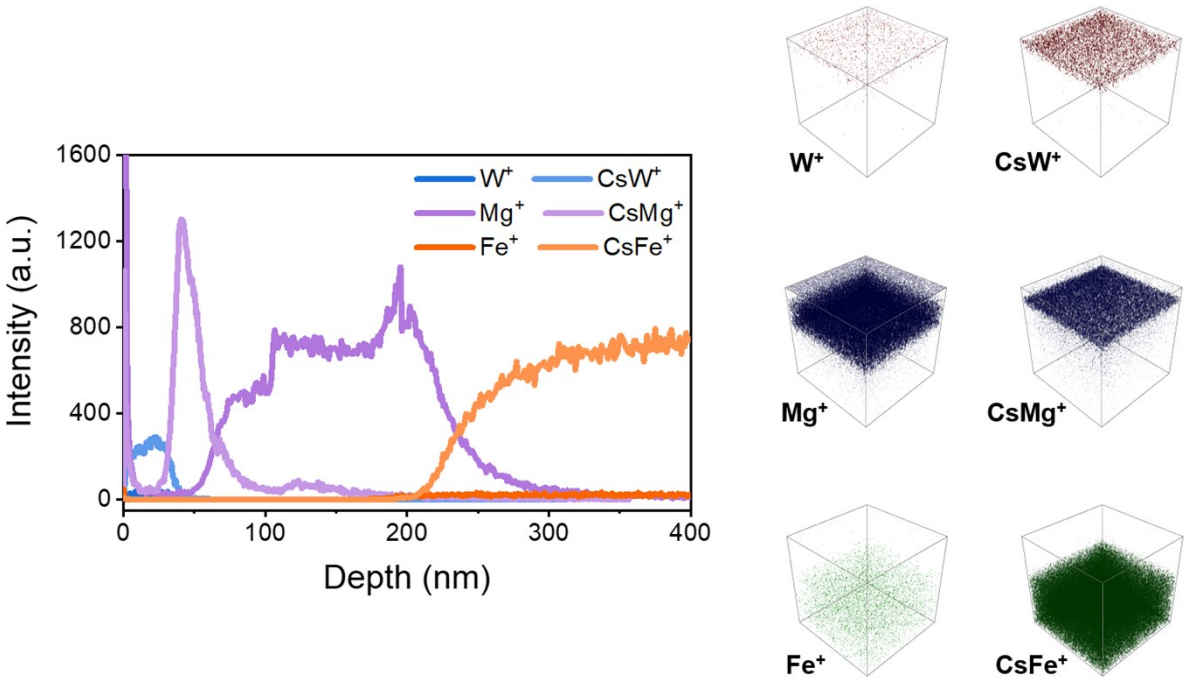

Fig. S4 ToF-SIMS depth profiles of the W/Mg thin-film electrode. The depth profiles reveal that the thicknesses of the W and Mg layers are approximately 30 nm and 200 nm, respectively. The SUS foil was used as the underlying current collector, and thus the onset of the Fe signal corresponds to the bottom of the corresponding W/Mg thin-film. The 30 nm thickness of the W layer is determined by the point at which the depth profiles of W and Mg intersect. A cesium (Cs)-based ion beam was utilized in the analysis, resulting in the detection of the corresponding Cs-containing peaks.

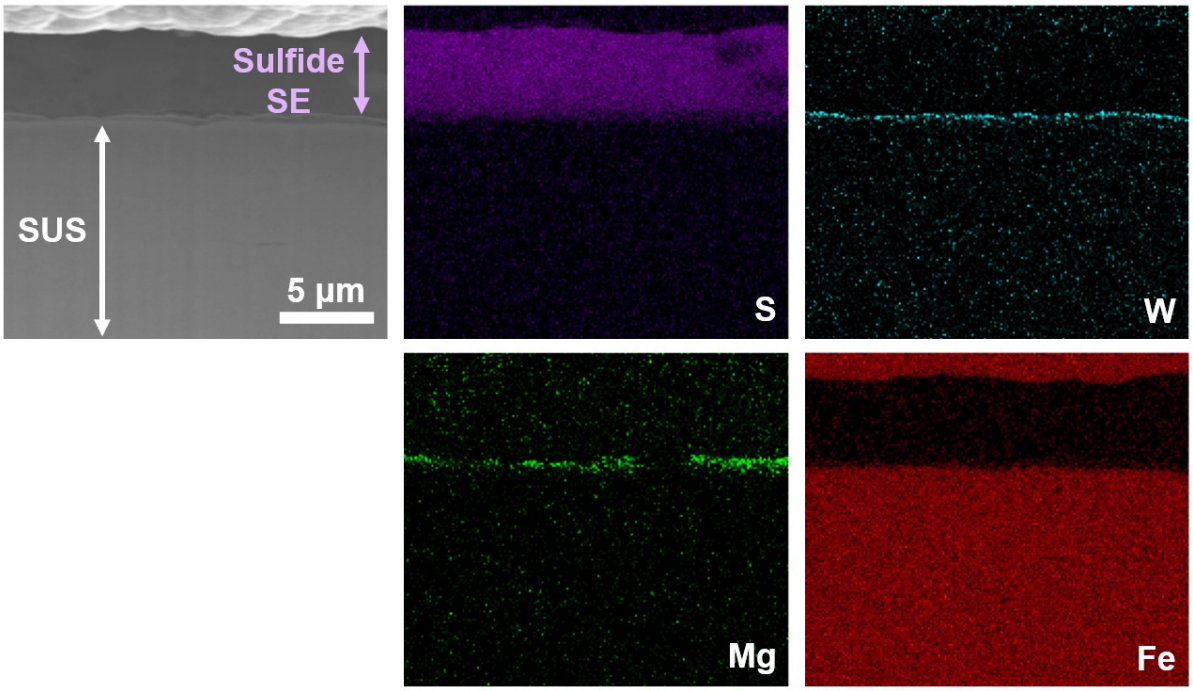

Fig. S5 Cross-sectional SEM-EDS images of the W/Mg thin-film electrode after the 1st Li plating-stripping. The structural integrity of the W/Mg bilayer persisted after one cycle of Li plating and stripping, indicating the sustainability of the film in contact with both the current collector and the SE layer.

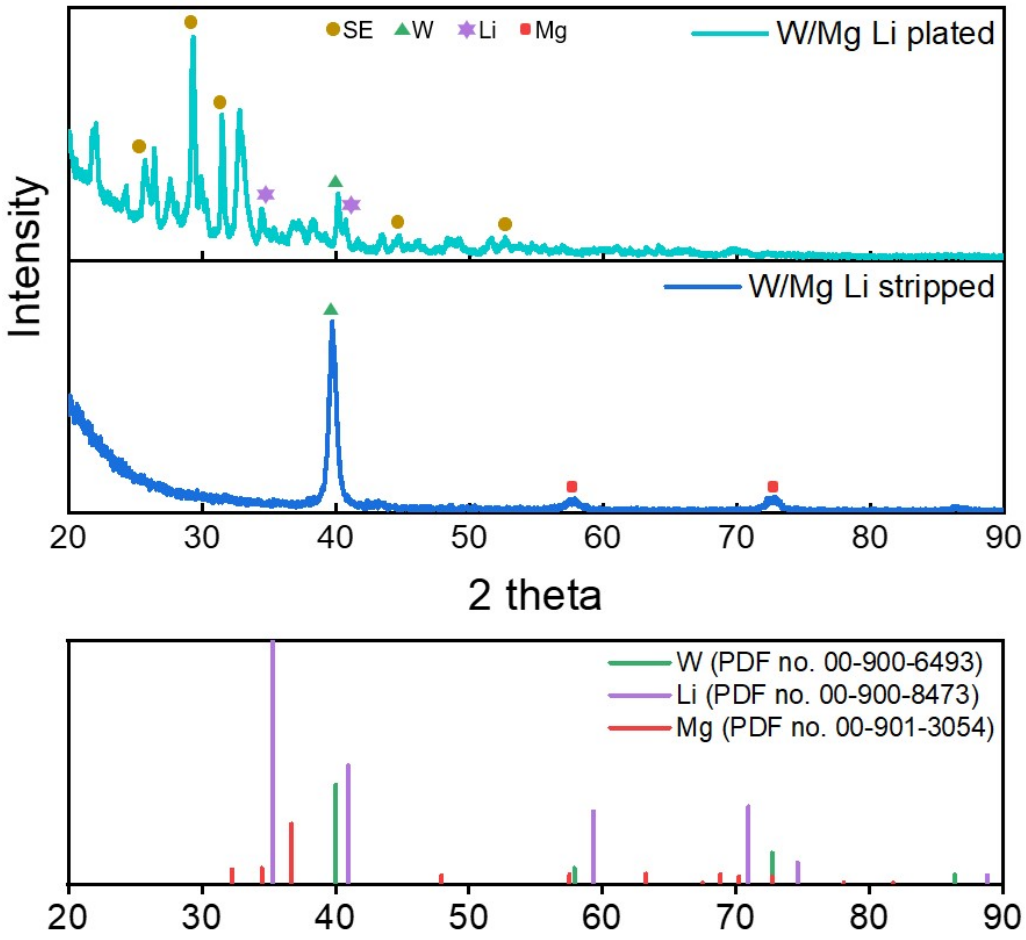

Fig. S6 XRD patterns of the W/Mg thin-film electrodes after Li plating and stripping. The persistence of the peak of crystalline W throughout Li plating and stripping implies that the W layer is inert towards Li. Additionally, in the case of the Li-deposited sample the complete removal of the SE was infeasible due to its adhesion to the deposited Li, explaining the presence of the sulfide SE peaks.

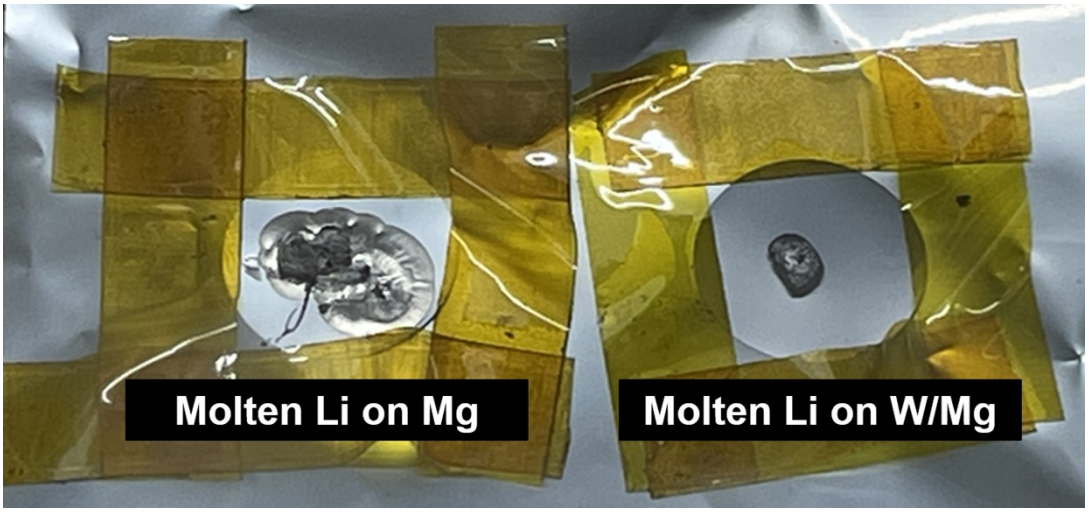

Fig. S7 Lithiophilicity and lithiophobicity test of Mg and W/Mg thin-film electrodes with molten Li. The assessment of the Li wettability of the thin-film electrodes entailed the deposition of molten Li onto both the Mg and W/Mg thin-film electrodes. Whereas the molten Li spread extensively over the Mg electrode, it did not wet the W/Mg electrode due to its strong cohesiveness.

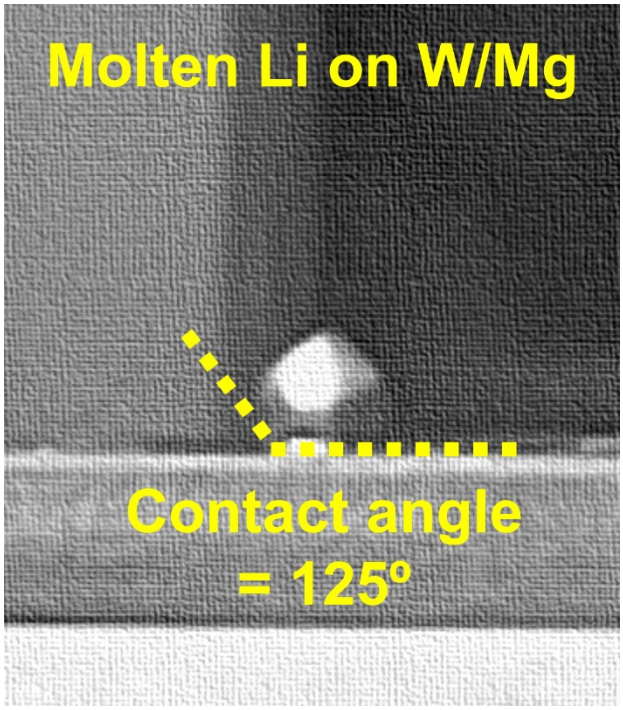

Fig. S8 Li wettability contact angle of the W/Mg thin-film electrode.

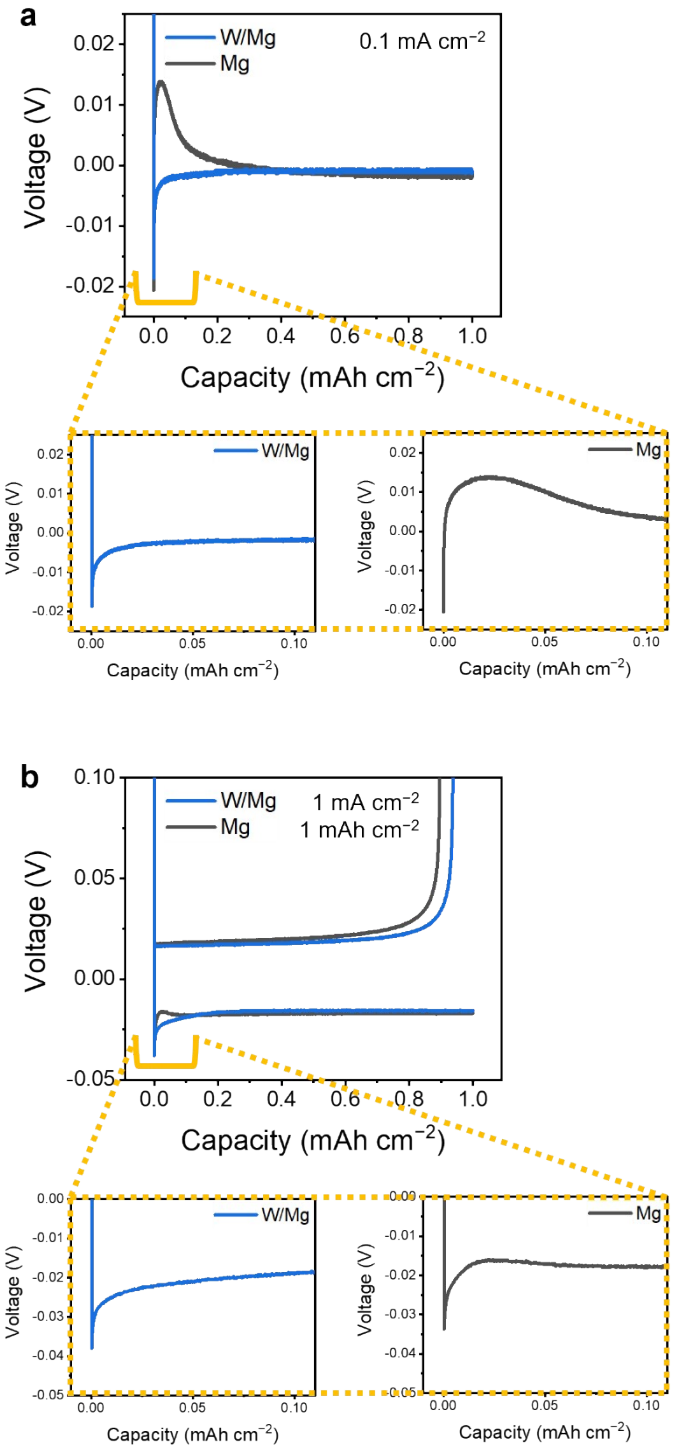

Fig. S9 Voltage profiles of Li plating-stripping of the thin-film electrodes. (a,b) Voltage profiles of the plating processes: (a) 0.1 mA cm^{-2} and 1 mAh cm^{-2}. (b) 1 mA cm^{-2} and 1 mAh cm^{-2}.

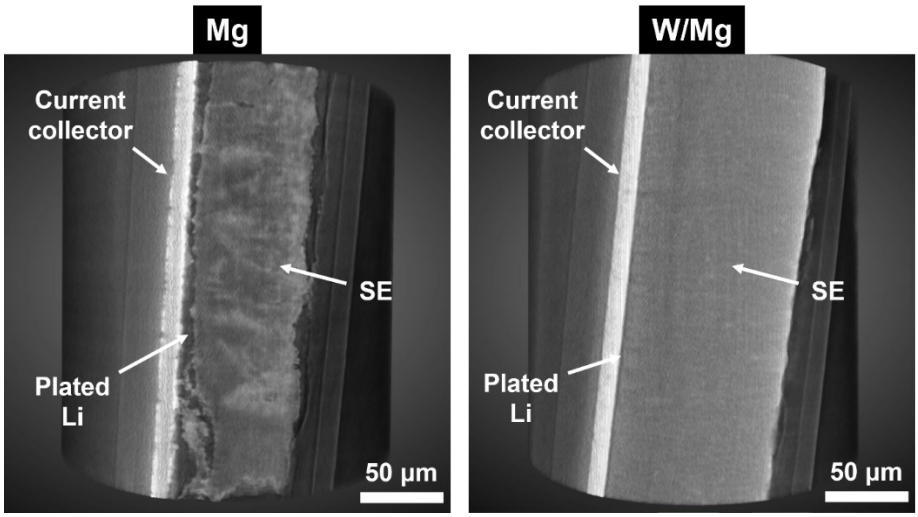

Fig. S10 XRM raw data of anode-SE interfaces using Mg and W/Mg thin-film electrodes after the 1st Li plating.

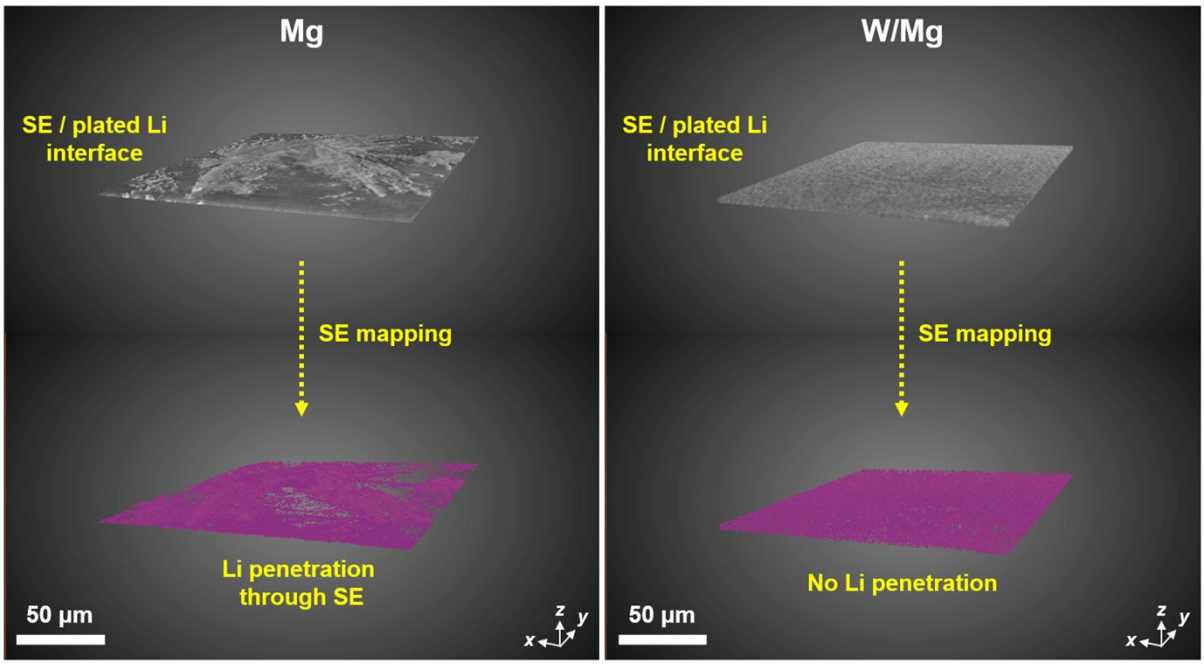

Fig. S11 3D XRM images of interfaces between the SE and Li deposits of the thin-film electrodes. For Mg, the SE layer (purple), extracted from the contrast, includes a significant amount of the Li, which reflects Li dendrite penetration into the SE layer. In contrast, the W/Mg sample has a much denser and flatter Li layer that is distinct from the SE layer.

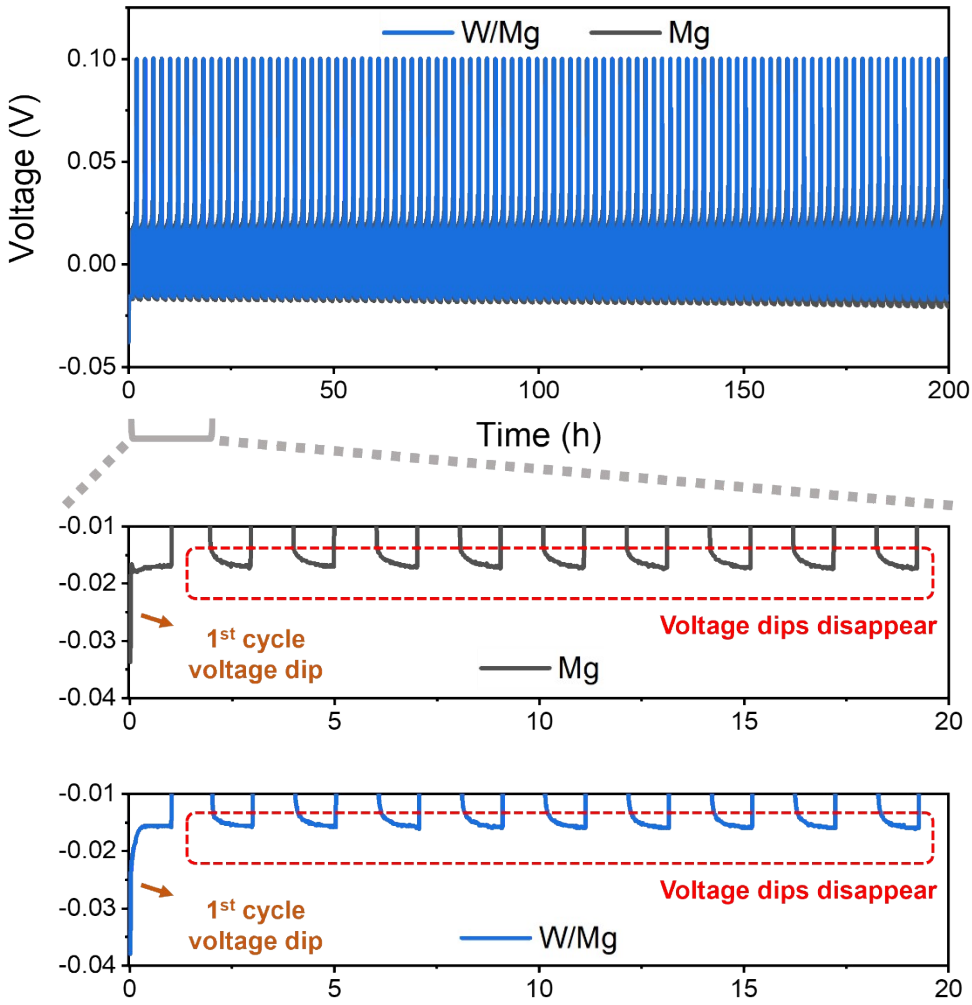

Fig. S12 Voltage-versus-time profiles of the thin-film electrodes during half-cell plating-stripping evaluation. The voltage dip observed in the first cycle, attributed to the Li nucleation overpotential, notably diminishes in subsequent cycles, and is indicative of the typical nucleation of Li on a lithiophilic substrate and the reduction of Li^{+} to Li^{0} at the Mg layer.

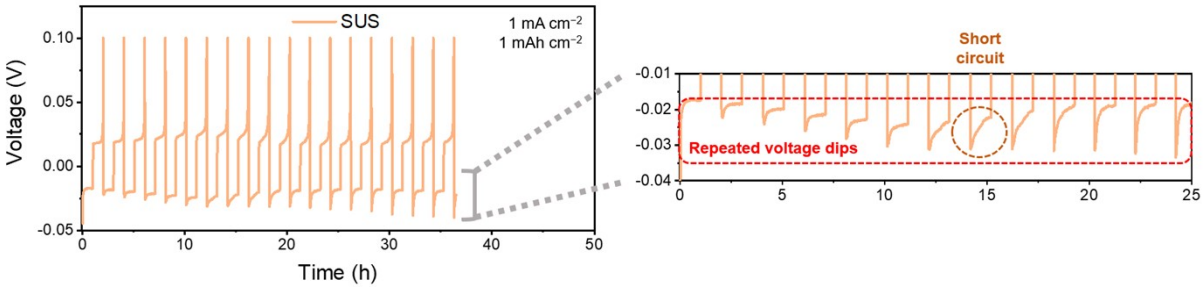

Fig. S13 Voltage profiles of half-cell plating-stripping tests with the bare SUS current collector, at a current density of 1 mA cm^{-2}, and with a capacity of 1 mAh cm^{-2}.

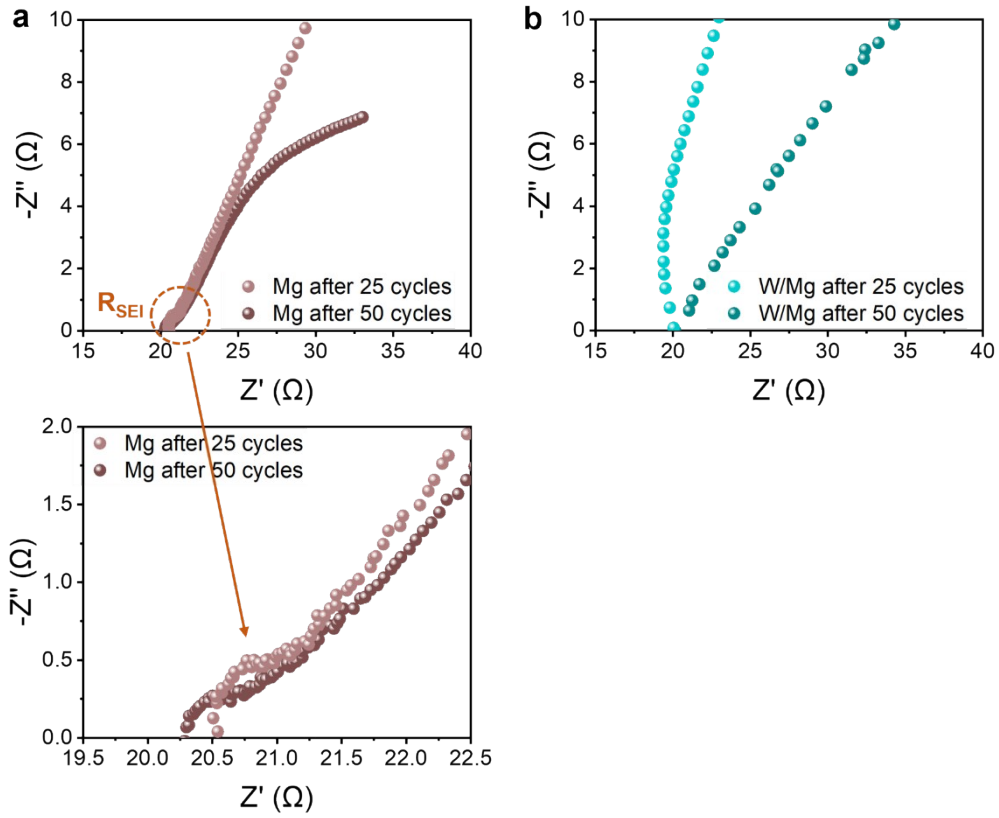

Fig. S14 EIS measurements during half-cell operation. Nyquist plots of the half-cells after 25 and 50 cycles, featuring (a) Mg and (b) W/Mg thin-film electrodes.

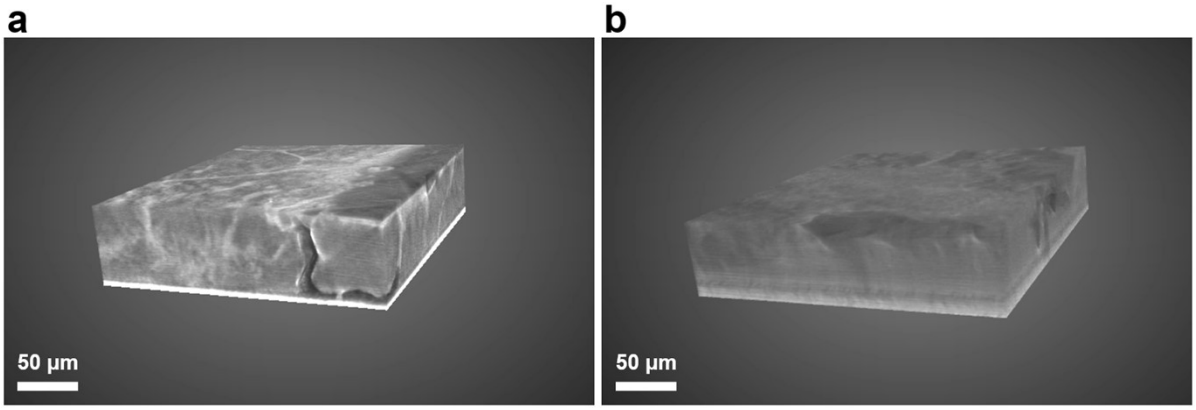

Fig. S15 XRM 3D raw data of anode-SE interfaces using (a) Mg and (b) W/Mg thin-film electrodes after 100 cycles of half-cell assessment.

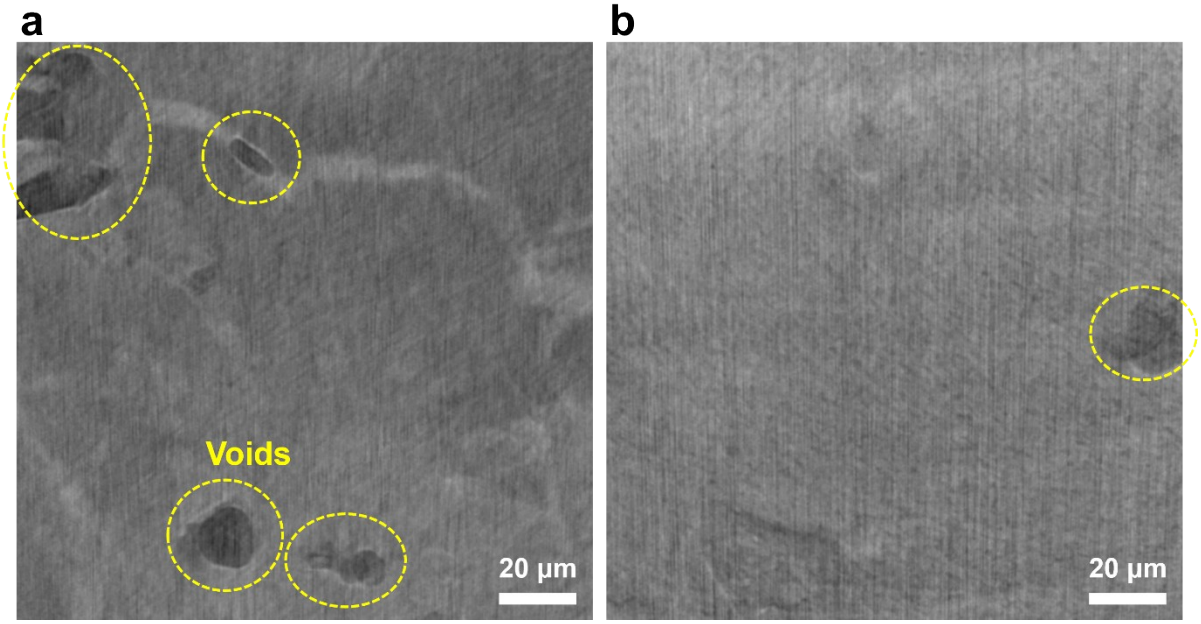

Fig. S16 2D XRM images of anode-SE interfaces following 100 cycles of half-cell evaluations, with (a) Mg and (b) W/Mg thin-film electrodes. For Mg, the conspicuous voids resulted from Li dendrite penetration at the interface, whereas W/Mg maintained a relatively smooth and uniform interface. This affirmed the effective inhibition of the growth of Li dendrites by the W layer.

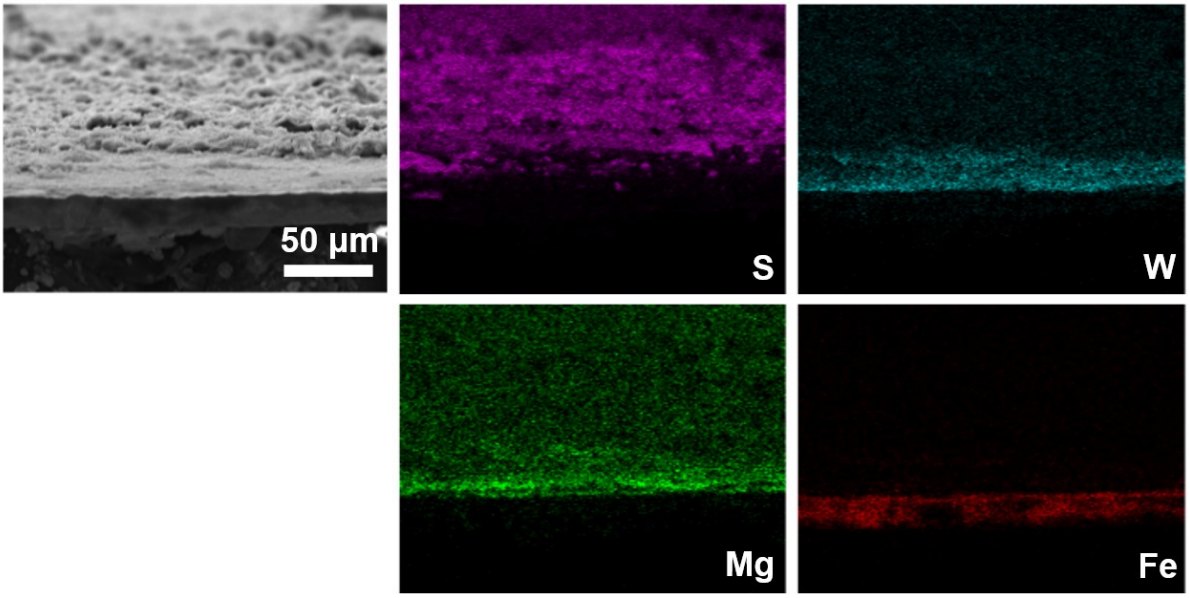

Fig. S17 Cross-sectional SEM-EDS images of the W/Mg thin-film electrode after 100 cycles of half-cell evaluation.

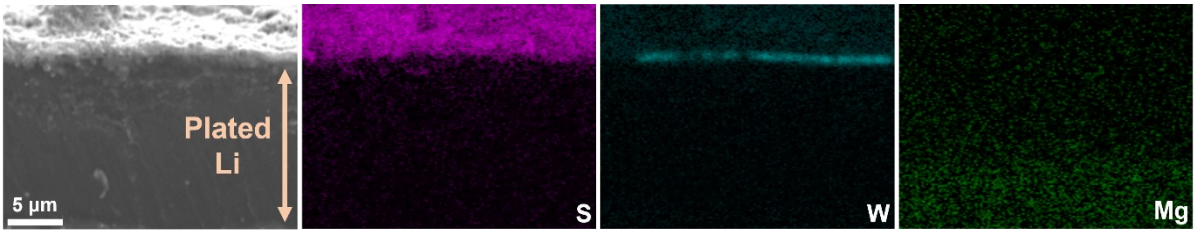

Fig. S18 Cross-sectional SEM-EDS images of the W/Mg thin-film electrode after the 101st Li plating during half-cell evaluation. 3 mAh cm^{-2} Li was plated following 100 cycles of operation at 1 mA cm^{-2} and 1 mAh cm^{-2}.

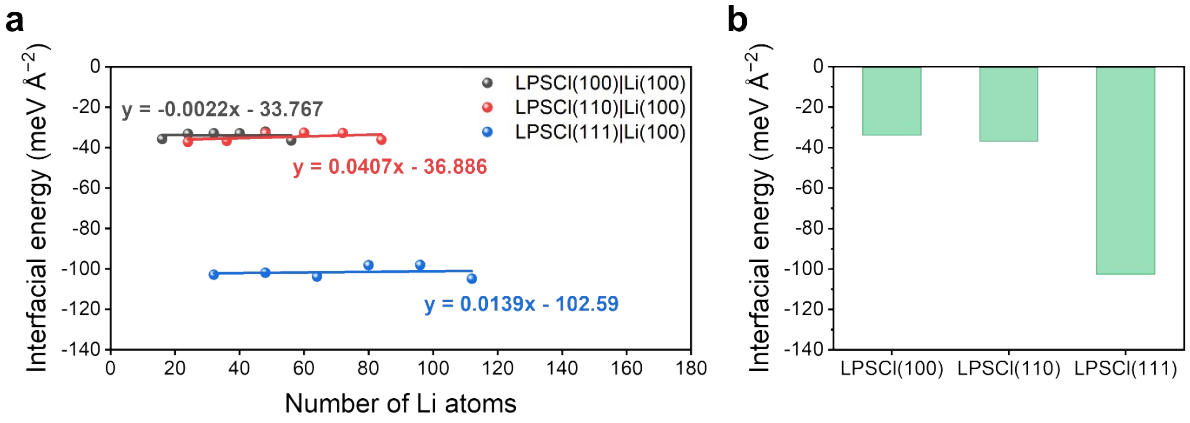

Fig. S19 DFT calculated interfacial energies between various planes of the LPSCl SE and Li (100) plane. Negative interfacial energies confirm the well-known occurrence of spontaneous redox reactions of SE upon making contact with Li, thereby leading to the reduction of the SE. The utilization of a material with such a low Li interfacial energy at the anode interface poses a risk, as it fails to impede Li dendritic growth[6,7]. This could potentially result in internal short circuits, a situation that is particularly critical under high current density conditions where charge concentration at the tip is heightened.

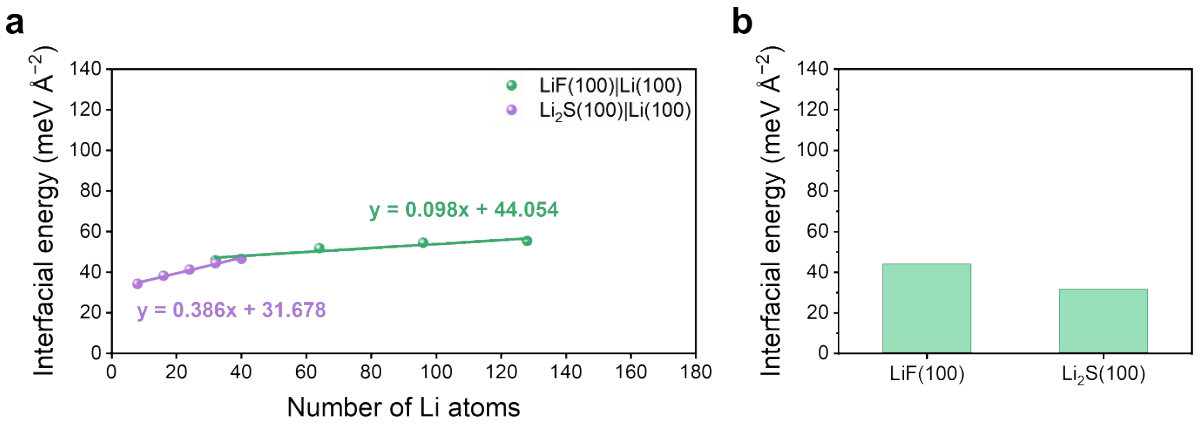

Fig. S20 Li interfacial energies of representative SEI components using DFT calculations. The Li interfacial energy values of Li_2S, a common SEI component in sulfide-based ASSBs, and LiF, a typical SEI component in LIBs, are both positive, and indicate the passivating nature of the SEI. Particularly, the higher value of LiF suggests its potential to inhibit the growth of Li dendrites, and has elicited widespread interest from researchers interested in forming LiF interfaces[8,9]. Nevertheless, interfacial materials with even higher Li interfacial energy are favorable to effectively suppress Li dendritic growth, especially under challenging conditions such as a thin protective layer and high current densities.

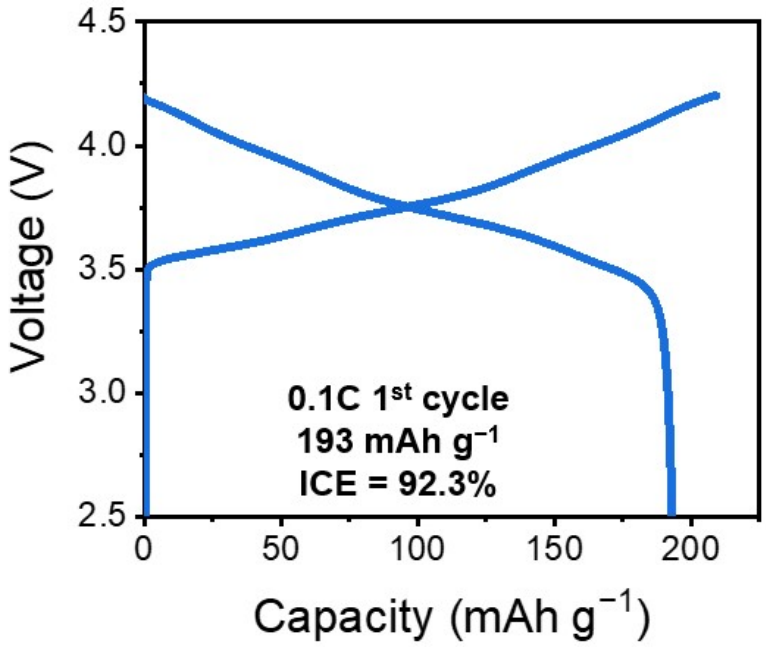

Fig. S21 Full-cell evaluation of the W/Mg thin-film anode paired with an NCM811 cathode. Voltage profile of the first-cycle of the W/Mg-based full-cell. ICE = 92.3%. Discharge capacity = 193 mAh g^{-1} based on the weight of the cathode active material.

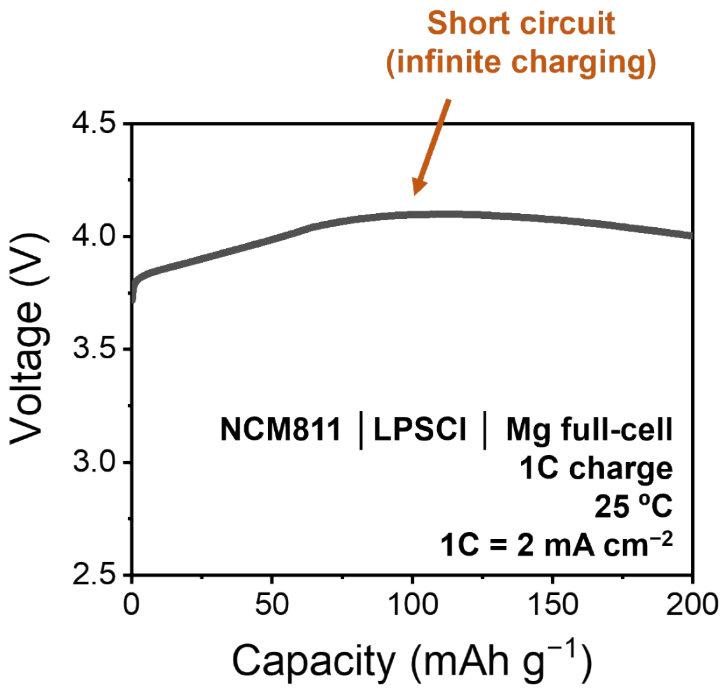

Fig. S22 Full-cell evaluation of the Mg thin-film anode paired with NCM811 cathode in the first cycle when charged at 1C. The infinite charging behavior is characteristic of internal short circuits.

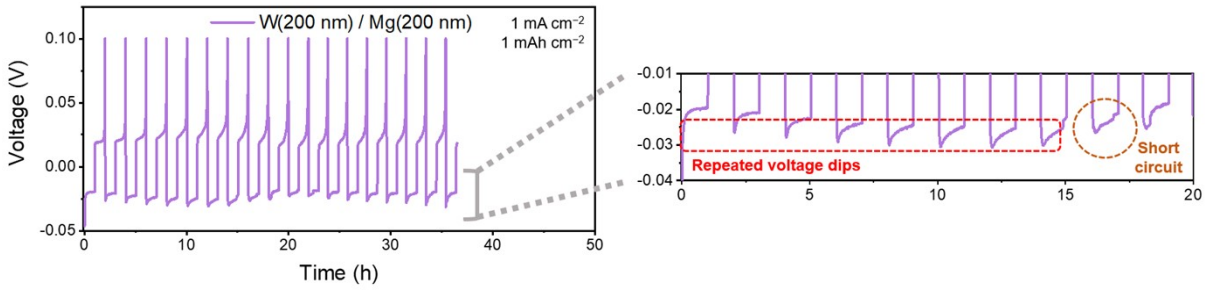

Fig. S23 Voltage profiles of half-cell plating-stripping tests with W(200 nm)/Mg(200 nm) thin-film anode, at a current density of 1 mA cm^{-2} and with a capacity of 1 mAh cm^{-2}. In the magnified view, repeated voltage dips appear throughout cycling.

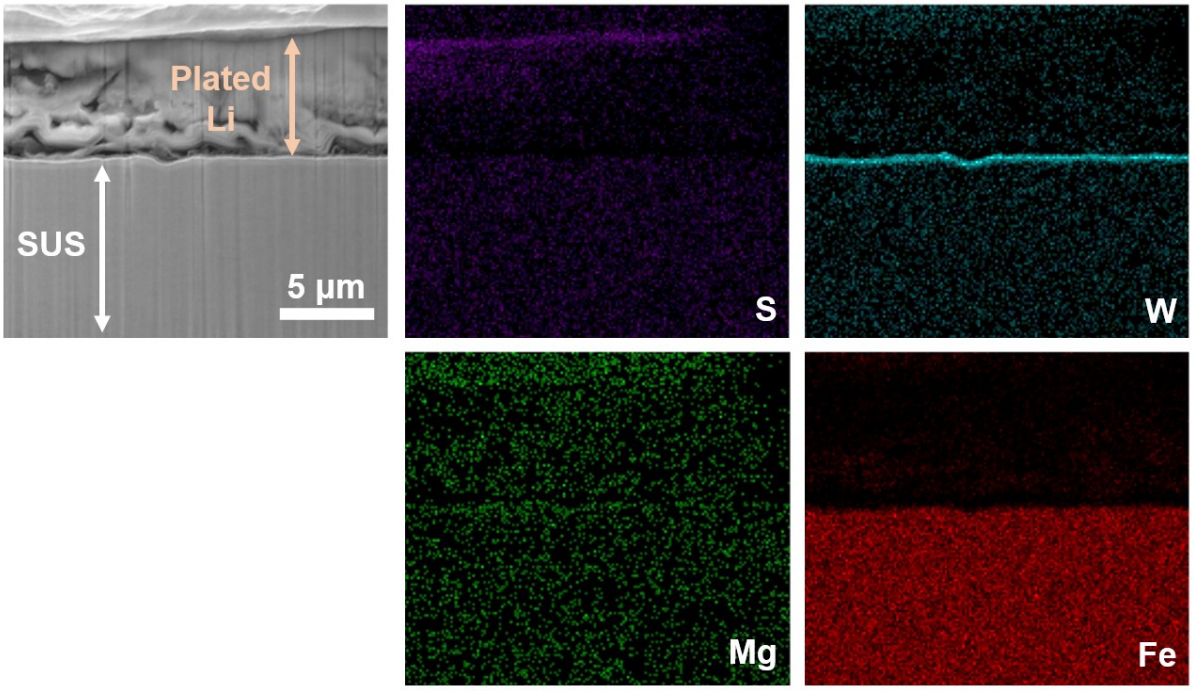

Fig. S24 Cross-sectional SEM-EDS images of the W(200 nm)/Mg(200 nm) thin-film anode after Li plating. The deposited Li was positioned above the W layer.

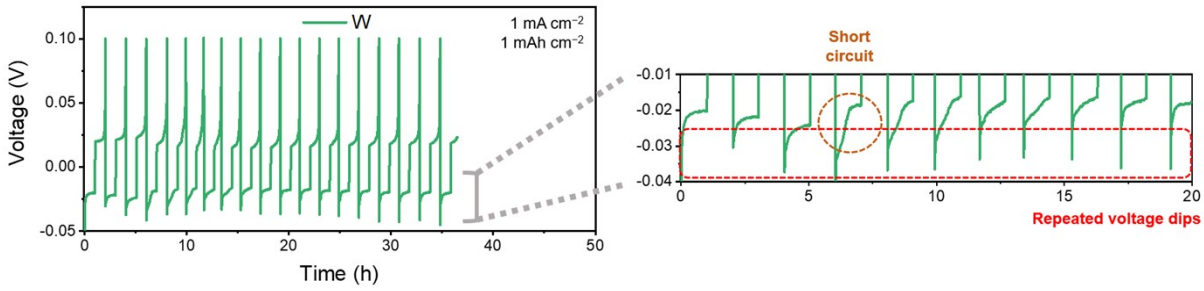

Fig. S25 Voltage profiles of the half-cell plating-stripping test with the W(30 nm) thin-film electrode without a Mg layer underneath (W(30 nm)/Mg(0 nm)) when cycled at a current density of 1 mA cm^{-2} and a capacity of 1 mAh cm^{-2}. In the magnified view, repeated voltage dips throughout the cycles are reflective of Li nucleation on the lithiophobic substrate.

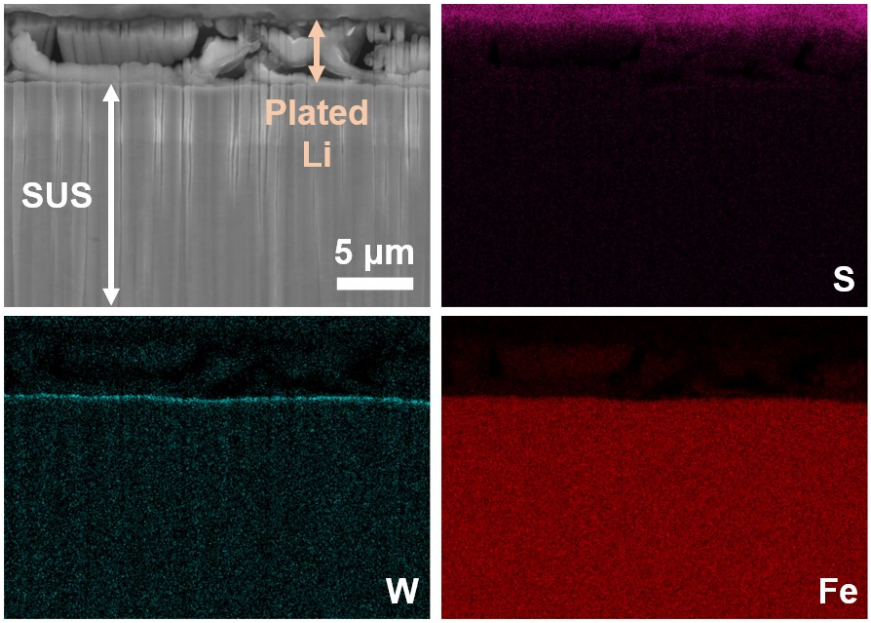

Fig. S26 Cross-sectional SEM-EDS images of the W(30 nm)/Mg(0 nm) thin-film electrode after Li plating.

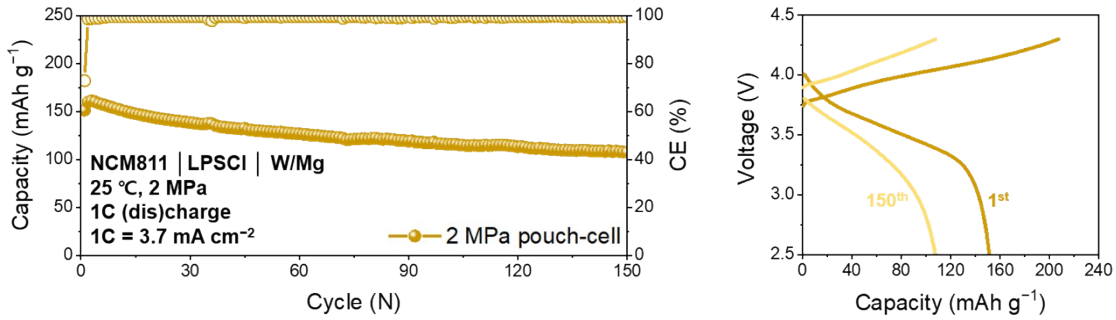

Fig. S27 Pouch-cell evaluations at a current density of 1C (1C = 3.7 mA cm^{-2}).

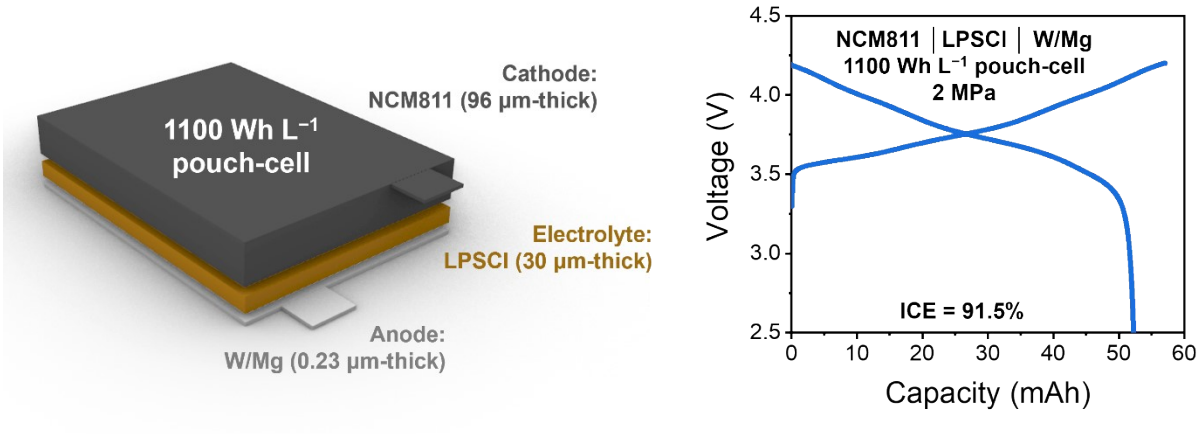

Fig. S28 High-energy density pouch-cell with volumetric energy density of 1100 Wh L^{-1}. Schematic representation featuring the thicknesses of individual layers (left) and the 1st voltage profile of the given pouch-cell at room temperature and a stack pressure of 2 MPa.

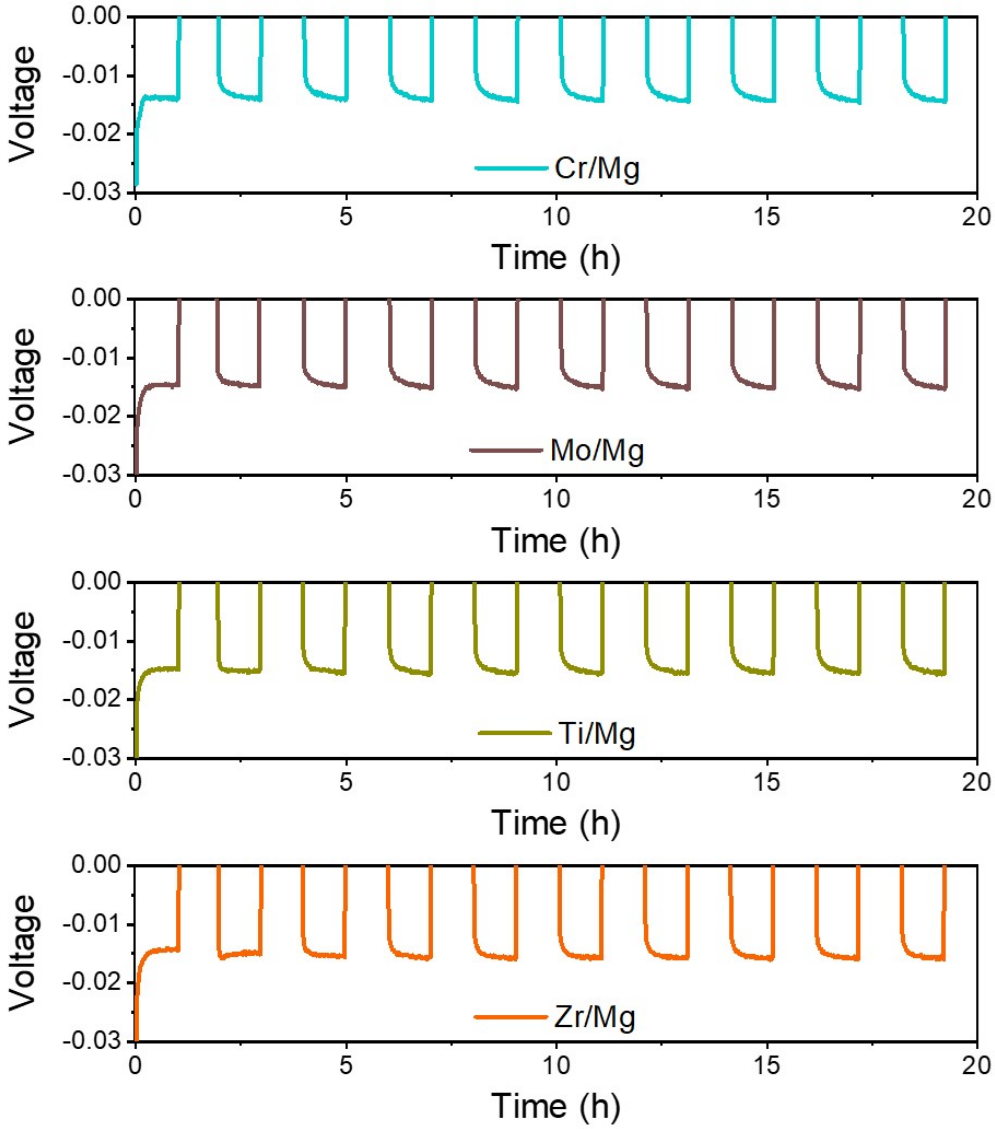

Fig. S29 Voltage vs. time profiles of the X(30 nm)/Mg(200 nm) thin-film electrodes (X = Cr, Mo, Ti, and Zr) during half-cell cycling involving Li plating-stripping. Thickness of the X layer = 30 nm. As is the case with W, Cr, Mo, Ti, and Zr do not form alloys with Li. Similar to the W/Mg system, we observed successful Li deposition on the Mg layer, as indicated by the absence of the voltage dips from the 2nd cycle onward.

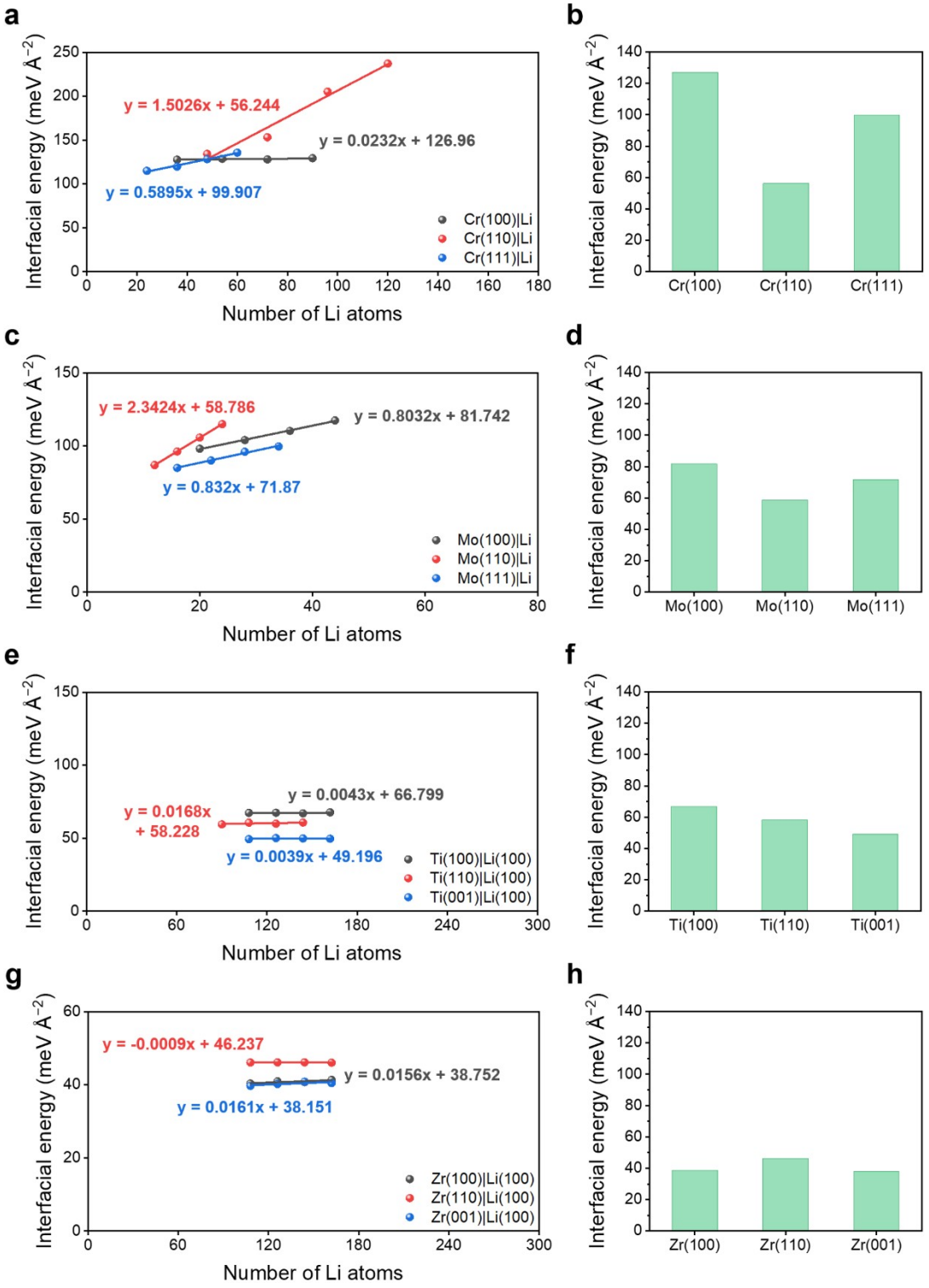

Fig. S30 DFT-calculated energies at the interface of Li with various lithiophobic metals. The high values of the calculated Li interfacial energies of Cr, Mo, Ti, and Zr, similar to that of W, indicate their potential for effectively mitigating Li dendritic growth. Therefore, similar to W, these metals can significantly enhance the CCD value of Li plating by precisely controlling the thickness at the nanoscale. It is worth noting that group 6 elements exhibit

relatively higher interfacial energies compared to those of group 4 elements. Hence, actively leveraging group 6 transition metals as a protective layer against Li appears to be an effective approach to achieve high (dis)charge current densities without the penetration of Li dendrites.

Table S1 Cell specifications for calculating the energy density of a W/Mg pouch cell.

Cathode	Thickness	96 μm
	Capacity	52.2 mAh
SE	Thickness	30 μm
Anode	**Thickness**	**0.23 μm**
Current collector	Al thickness	12 μm
	Ni thickness	10 μm
Total thickness		148.23 μm
Area		4X3 cm^2
Nominal discharge voltage		3.75 V
Energy density		**1100 Wh L^{-1}**

References

1. G. Kresse and J. Furthmüller, *Comput. Mater. Sci.*, 1996, **6**, 15-50.
2. J. P. Perdew, K. Burke and M. Ernzerhof, *Phys. Rev. Lett.*, 1996, **77**, 3865-3868.
3. P. E. Blöchl, *Phys. Rev. B*, 1994, **50**, 17953-17979.
4. N. D. Lepley and N. A. W. Holzwarth, *Phys. Rev. B*, 2015, **92**, 214201.
5. X. Wu, Y.-W. You, X.-S. Kong, J.-L. Chen, G. N. Luo, G.-H. Lu, C. S. Liu and Z. Wang, *Acta Mater.*, 2016, **120**, 315-326.
6. X. Ji, S. Hou, P. Wang, X. He, N. Piao, J. Chen, X. Fan and C. Wang, *Adv. Mater.*, 2020, **32**, 2002741.
7. X. Fan, X. Ji, F. Han, J. Yue, J. Chen, L. Chen, T. Deng, J. Jiang and C. Wang, *Sci. Adv.*, 2018, **4**, eaau9245.
8. T. Li, X.-Q. Zhang, P. Shi and Q. Zhang, *Joule*, 2019, **3**, 2647-2661.
9. Y. Liu, X. Tao, Y. Wang, C. Jiang, C. Ma, O. Sheng, G. Lu and X. W. Lou, *Science*, 2022, **375**, 739-745.